PCCP

Accepted Manuscript

ROYAL SOCIETY OF CHEMISTRY

www.rsc.org/pccp

Physical Chemistry Chemical Physics
CREATED USING THE RSC LaTeX PCCP ARTICLE TEMPLATE – SEE www.rsc.org/electronicfiles FOR DETAILS
ARTICLE TYPE www. rsc.org/xxxxxx | XXXXXXXX

Effective coarse-grained solid-fluid potentials and their application to model adsorption of fluids on heterogeneous surfaces†

Esther Forte,[a,b] Andrew J. Haslam,[a,c], George Jackson[a] and Erich A. Müller[a,*]

Received Xth XXXXXXXXXX 20XX, Accepted Xth XXXXXXXXX 20XX
First published on the web Xth XXXXXXXXXX 200X
DOI: 10.1039/b000000x

The use of effective fluid-surface potentials, in which the full position-dependent potential is replaced by a potential that depends only on the distance from the surface of the solid, is a common practice as a route to reduce the complexity of evaluating adsorption of fluids on substrates. Conceptually this is equivalent to replacing the detailed description of the discrete molecular nature of the solid by a coarse-grained description in which the solid is represented by a continuous (structureless) surface. These effective fluid-surface potentials are essential in the development of theories for surface adsorption, and they provide a means to reduce the computational cost associated with molecular simulation of the system. The main purpose of the present contribution is to emphasise the necessity of using an adequate averaging procedure to obtain effective fluid-surface potentials. A simple unweighted average of the configurational energy is commonly employed resulting in effective potentials that are temperature independent. We describe here a procedure to develop free-energy-averaged effective fluid-surface potentials retaining the important temperature dependence of the coarse-grained interaction between the particle and the surface. Although the approach is general in nature, we assess the merits of free-energy-averaged potentials for the adsorption of methane on graphene and graphite, making appropriate comparisons with the description obtained with the traditional temperature-independent potentials. Additionally, we develop effective fluid-surface potentials for crystalline faces of monolayer and multilayer homogeneous and heterogeneous fcc lattices based on the Lennard-Jones (12-6) pair potential, and compute the corresponding adsorption isotherms of Lennard-Jones fluids on these surfaces using Grand Canonical Monte Carlo (GCMC) simulations. The adequacy of two different options to obtain effective fluid-surface potentials (a free-energy-based versus a simple unweighted average) is critically compared. It is shown here that the higher the heterogeneity of the surface the less adequate simple unweighted averages are to describe the adsorption behaviour in comparison to free-energy averages.

1 Introduction

The first successful attempts to develop a theory of surface adsorption date back almost a century, with the contributions of Polanyi[1,2] and Langmuir[3]. In contrast to the approach of Langmuir, who explained adsorption based on a chemical formalism, Polanyi supported the description of adsorption as a physical process, in which the adsorption can be explained in terms of an adsorption potential defined as the work done in bringing a molecule from the gas phase to a point near the adsorbent[4]. Polanyi's picture of adsorption established an important basis for modern theories[5–7]. In spite of its rigorous molecular foundation, the modern application of adsorption theories has a marked empirical nature. Significant inadequacies can be found revisiting approaches that describe surface adsorption and a reflection of this is the general difficulty encountered in reproducing the experimental temperature dependence of adsorption data, requiring the use of temperature-dependent energetic adsorption parameters to describe different adsorption isotherms (see refs. 8–16 for some recent examples). Some of these flaws can be traced to a poor understanding of the effect of temperature in fluid-surface potentials; here we are referring to effective potentials whereby the interaction of a fluid molecule with an explicit surface is expressed using a coarse-grained or homogeneous wall representation of a solid.

There has been a considerable amount of work published on the subject of the explicit dependence of average interaction energies with temperature. The "potential of the average force" considered by Onsager[17], along with the work of Rushbrooke[18] on temperature dependent effective interactions are worth a particular mention in this context. The importance of using an average free-energy as the correct approach to describe effective potentials that are based on integrating out

† Electronic Supplementary Information (ESI) available: See DOI: 10.1039/b000000x/

[a] *Department of Chemical Engineering, Imperial College London, London SW7 2AZ, UK.*
[b] *BP Centre for Petroleum and Surface Chemistry (BP-CPSC), Department of Chemistry, University of Surrey, Guildford GU2 7XH, UK.*
[c] *Qatar Carbonates and Carbon Storage Research Centre (QCCSRC), Imperial College London, London SW7 2AZ, UK.*
* Corresponding author's email: e.muller@imperial.ac.uk

variables that are not of interest, such as angles in the case of polar interactions, is now well established (see, for example, refs.[19–26]). Effective potentials of this type can be developed by ensuring that the partition function of the integrated representation is equal to that of the explicit system: the effective potential determined in this way will be equivalent to a free energy, and as a consequence are often referred to as free-energy-averaged potentials.

Free-energy averages are frequently employed to describe fluid-fluid interactions. A seminal example is the orientation-independent or angle-averaged free energy of the dipolar interactions which lead to the well known Keesom interaction[26,27] through an expansion and truncation of the expression of the free-energy. It is interesting to note that the work of Keesom dates back to 1921, prior to the more rigorous statistical mechanical analysis of Rushbrooke[18]. The use of orientation-independent fluid-fluid potentials is possibly the most extended application of free-energy-averaged potentials, as an approach to link the free energy of the explicit system to that of a system with fewer degrees of freedom. This type of averaging is commonly employed to obtain the reference-system potential in the so-called Reference Average Mayer-Function (RAM) perturbation theory[28], as well as in other perturbation theories[22,29,30]. The reader is referred to the excellent reviews given in refs 31–34. In the work of Zwanzig[35], which is recognised as one of the first attempts to develop a perturbation theory for dense fluids[34], the free-energy average is expressed as a high-temperature expansion. The development of a perturbative free energy as a high-temperature series had previously been shown by Peierls[36,37] in a study devoted to the theory of diamagnetism, where much of the basis of modern perturbation theory is set[32]. Further applications of perturbation theory to polar fluids are found, where angle-averages about a non-polar reference system are again employed, wherein the effects of polarisability as well as permanent dipoles[29,38–40] and higher multipoles[23,41,42] are included as a perturbation. This body of work contributed to the establishment of the general features of coarse-grained averages of the free energy and their temperature dependence in the form of a high-temperature series expansion. Free-energy average potentials are also widely used to describe the effective interactions in colloidal, polymeric and biomolecular systems[43–46].

In spite of the state of maturity in the application of free-energy averages within the field of bulk fluid interactions, to our knowledge its extension to effective potentials for fluid-surface interactions is generally overlooked. Effective fluid-surface potentials are typically obtained through a simple sum of the pair interaction u_{ij} of the fluid particle i with each wall atom j, i.e., the particle-wall energy $U = \sum_j u_{ij}$ is averaged over a number of configurations (see for example refs. 26,47,48). This effective potential, which we denote as the unweighted average $\langle U \rangle$, is thereby determined as $\langle U \rangle = \frac{1}{N_{\text{cnf}}} \sum_{k=1}^{N_{\text{cnf}}} U$, over N_{cnf} configurations. This type of classical approach of obtaining effective fluid-surface potentials of a given adsorbate molecule i with a wall has largely ignored the temperature dependence of the resulting average potential. In practice the explicit structure of the wall is ignored in the theoretical development and the sum is replaced by an integration. The result of integrating an intermolecular interaction which is proportional to an inverse power of the distance r as $1/r^n$ for the average interaction between a molecule and a macroscopic solid of dimensionality d results in an interaction potential which varies as $1/r^{n-d}$. This dependence was already known to Newton[49] in 1686 when he solved the problem of determining the attractive force with which a corpuscle is attracted by an infinite plane in two dimensions. At the beginning of the 19th century, numerous authors[4] focused on deriving expressions for the interactions of a gas molecule with a solid surface from more explicit molecular considerations, attributed to polar and/or electrostatic effects. London[50] was the first[4] to recognise and incorporate the importance of the attractive dispersion interactions in 1930. Considering a dispersion potential between a gas molecule and an atom or molecule in the adsorbent given by a power law of the $-C/r^6$, London[50] assumed that the distances between the adsorbent atoms were small compared with the distances between the gas molecule and the adsorbent atoms, obtaining an average particle-surface interaction of $-M\pi C/6r^3$ by integrating over an infinite surface, with M being the number of adsorbent molecules per unit volume. For the (12-6) Lennard-Jones (LJ) intermolecular interaction, the result of integrating over a single-layer LJ solid is a (10-4) potential, and over a multilayered solid is a (9-3) potential (an early reference to this integrated potential is given by Hill[51] in 1948). It was shown by Steele that the latter potential does not provide an accurate approximation for a multilayered solid[52], leading him to develop the now ubiquitous (10-4-3) potential[48,52,53]. Both, the (9-3) and the (10-4-3) potential, are widely used in the modelling of adsorption for flat surfaces, and analogous potentials have been developed for spherical, cylindrical and other pore geometries[54–58], and to account for polar interactions[59]. In spite of their widespread use, these potentials are temperature independent, and, as will be shown in our current contribution, are often not appropriate to describe adsorption at moderate and low temperatures.

It is our purpose to explain in detail how effective free-energy-averaged potentials w are obtained through an equality in the corresponding Boltzmann factors. In his work with surfaces at low temperature, Abraham[60] noted that a (10-4) potential was a poor effective potential for the (100) structured surface. He suggested that the probability that a single atom interacting with a given wall is at a given position (x,y,z) is proportional to $\exp(-U(x,y,z)/k_{\text{B}}T)$, where $U(x,y,z)$ is the interaction energy

at that position, and a "Boltzmann-weighted" effective interaction $w(z)$ based on a structureless integration of the potential over a surface was proposed:[60]

$$\exp\big(-\beta w(z)\big) = \frac{1}{a_u}\int_{a_u} \exp\big[-\beta U(x,y,z)\big]\mathrm{d}x\mathrm{d}y, \qquad (1)$$

where a_u is the area of the unit cell of the solid surface, $\beta = 1/k_B T$ and k_B is Boltzmann's constant. As will be shown later in our contribution, in the formal procedure of obtaining free-energy-averaged potentials, the integration (or sum) is not restricted to one unit cell of the solid but to the entire volume (or area, in the case of a single surface monolayer) within which fluid and solid particles interact.

It should be noted that these free-energy averages are different to canonical (or confusingly named Boltzmann) averages w', as discussed elsewhere[18,20,61]. The expression to obtain an effective potential describing the interaction of a fluid particle with a solid through a canonical average over N configurations is given by

$$w' = \frac{\sum_{k=1}^{N} U\exp(-\beta U)}{\sum_{k=1}^{N}\exp(-\beta U)}. \qquad (2)$$

This potential does not, however, ensure that the partition function, and thereby the free energy, of the effective coarse-grained system is identical to that of the explicit system. Canonical averages have also been suggested for angle-averaged potentials to describe the interaction between guest and host molecules in gas hydrates[8,62], although, as commented by Trout and coworkers[8,62], the approach lacks of a rigorous justification.

Here, we demonstrate that a free-energy-averaged potential is essential to describe adsorption on the surface of very heterogeneous solids at low and moderate temperature in an appropriate manner. We will not assume structureless solids, calculating the effective potentials by accounting for the pair interactions of a fluid particle with every particle of the solid arranged in a given ordered lattice.

Our manuscript is arranged as follows: The procedure employed to map the explicit with continuum descriptions of the solid through the appropriate free energy averages is given in the next section. For this a structureless solid is considered first, and so the methodology will be based on integrations over the solid. This allows one to establish a link between the effective potentials obtained and those typically used such as the (9-3) potential. The development of the effective free-energy surface potentials is then explained in detail for solids with a given structure. A comparison of the use of these free-energy-averaged potentials with other effective potentials is then made to assess their adequacy in describing surface adsorption on different solid lattices based on Grand Canonical Monte Carlo simulation results.

2 Methodology

2.1 Free energy mapping of explicit and continuum descriptions of the fluid-solid interaction

Considering a single fluid particle interacting with a solid, an expression for the effective free-energy-averaged potential can be obtained by mapping a coarse-grained continuum-wall representation of the system to the atomistic discrete description. This mapping is done by equating the partition function for both levels of resolution at a certain fluid-wall or, equivalently, fluid-surface distance.

If we assume that the discrete solid consists of M particles, the canonical partition function of this system consisting of a single fluid particle in the vicinity of the surface of such a solid is given by

$$Q = F_s(T)F_f(T)\int d\mathbf{r}_f \int d\mathbf{r}_s^M \exp\left(-\frac{U(\mathbf{r}_s^M,\mathbf{r}_f)}{k_B T}\right), \qquad (3)$$

where $F_s(T)$ and $F_f(T)$ are functions of temperature representing the kinetic degrees of freedom (corresponding to de Broglie-like volumes) of the solid and fluid particles, respectively, and U is the total intermolecular potential. We can define a new distance, $\mathbf{r}_{fs}$ relative to the position of the fluid particle (see Figure 1):

$$\mathbf{r}_{fs} = \mathbf{r}_s - \mathbf{r}_f \qquad (4)$$

and integrate out the explicit dependence of the particle's position so that

$$Q = F_s(T)F_f(T)V_f\int d\mathbf{r}_{fs}^M \exp\left(-\frac{U(\mathbf{r}_{fs}^M)}{k_B T}\right), \qquad (5)$$

where V_f is the volume accessible to the fluid particle. If the solid wall is at a distance D from the fluid molecule we can

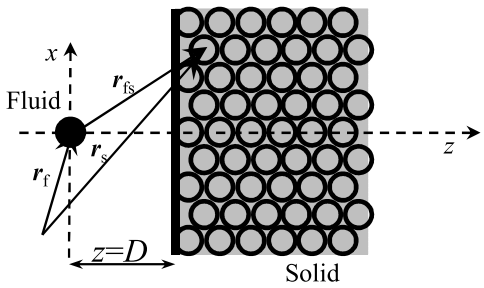

Fig. 1 Schematic of the relative positions between an adsorbed fluid molecule and a given particle in the solid. The surface of the solid is represented at a distance $z = D$.

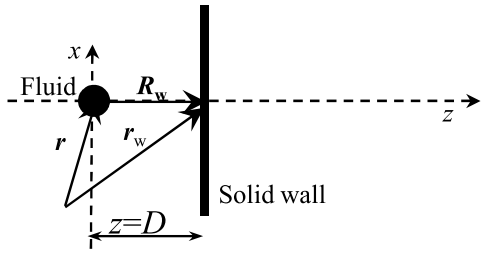

Fig. 2 Schematic of the relative positions between an adsorbed fluid molecule and a continuum solid surface or wall which is represented at a distance $z = D$.

express the partition function at D as follows

$$Q(D) = F_s(T)F_f(T)V_f \times \int_{-\infty}^{+\infty} dx_{fs}^M \int_{-\infty}^{+\infty} dy_{fs}^M \int_{D}^{+\infty} dz_{fs}^M \exp\left(-\frac{U(x_{fs}^M, y_{fs}^M, z_{fs}^M)}{k_B T}\right), \quad (6)$$

where the distance normal to the surface is represented by the z axis. From the partition function, the Helmholtz free energy A (or more strictly a Landau free energy, e.g., see ref. 63) can be obtained as

$$A(D) = -k_B T \ln Q(D). \quad (7)$$

If on the other hand we consider a coarse-grained system represented by a continuum wall again normal to the z direction (see Figure 2), the partition function of this system is described by

$$Q_{CG} = F_f(T) \int d\mathbf{r} \int dz_w \exp\left(-\frac{w(\mathbf{r}, z_w)}{k_B T}\right), \quad (8)$$

where w is the coarse-grained fluid-surface potential of the particle with the wall. If, as before, distances are expressed relative to the fluid particle ($\mathbf{R}_w$), the surface potential will then only depend on the perpendicular distance to the plane ($\mathbf{R}_w = Z$)

$$Q_{CG} = F_f(T)V_f \int dZ \exp\left(-\frac{w(Z)}{k_B T}\right). \quad (9)$$

On considering an infinitely thin wall for a fluid-wall distance of $Z = D$, the only position at which $w(Z)$ will take a value different from zero will be $Z = D$. The sharp dependence with Z can be then represented in terms of a delta function, so that

$$\begin{aligned} Q_{CG}(D) &= F_f(T)V_f \int_0^{+\infty} dZ \exp\left(-\frac{w(Z)}{k_B T}\right)\delta(Z-D) \\ &= F_f(T)V_f \exp\left(-\frac{w(D)}{k_B T}\right). \end{aligned} \quad (10)$$

The mapping between explicit and coarse-grained potentials follows by equating the free energy, or equivalently, the partition function of both systems [Eqs. (6) and (10)]

$$Q_{CG}(D) = Q(D), \quad (11)$$

whereby we have

$$\exp\left(-\frac{w(D)}{k_B T}\right) = F_s(T) \int_{-\infty}^{+\infty} dx_{fs}^M \int_{-\infty}^{+\infty} dy_{fs}^M \int_{D}^{+\infty} dz_{fs}^M \times \exp\left(-\beta U(x_{fs}^M, y_{fs}^M, z_{fs}^M)\right). \quad (12)$$

To simplify the expression, the inverse temperature is expressed as $1/(k_B T) = \beta$. One can continue by expanding the exponential ($\exp(x) = \sum_{i=0}^{\infty} x^i/i!$) on the right-hand side of Equation (12) as follows

$$\exp\left(-\frac{w(D)}{k_B T}\right) = F_s(T) \int_{-\infty}^{+\infty} dx_{fs}^M \int_{-\infty}^{+\infty} dy_{fs}^M \int_{D}^{+\infty} dz_{fs}^M \times \left[1 - \beta U(r_{fs}^M) + \frac{\beta^2}{2} U^2(r_{fs}^M) + \mathcal{O}(U^3)\right]. \quad (13)$$

Assuming pairwise additive potentials,

$$U = \sum_{i=1}^{M} u(r_{fs,i}), \quad (14)$$

we have

$$\begin{aligned} \exp\left(-\frac{w(D)}{k_B T}\right) = F_s(T) &\times \left[V_s^M - \beta \int_{-\infty}^{+\infty} dx_{fs}^M \int_{-\infty}^{+\infty} dy_{fs}^M \int_{D}^{+\infty} dz_{fs}^M \sum_{i=1}^{M} u(r_{fs_i}) \right. \\ &+ \frac{\beta^2}{2} \int_{-\infty}^{+\infty} dx_{fs}^M \int_{-\infty}^{+\infty} dy_{fs}^M \int_{D}^{+\infty} dz_{fs}^M \sum_{i=1}^{M} \sum_{j=1}^{M} u(r_{fs_i}) u(r_{fs_j}) \\ &\left. + \mathcal{O}(u^3)\right], \end{aligned} \quad (15)$$

where V_s is the volume occupied by the solid. The expression can be further approximated by considering a solid of uniform

density $\rho_s = {}^{M}/_{V_s}$, so that one can write

$$\exp\left(-\frac{w(D)}{k_B T}\right) = F_s(T)\Bigg\{V_s^M - \beta M V_s^{M-1} \times \int_{-\infty}^{+\infty} dx_{fs_1} \int_{-\infty}^{+\infty} dy_{fs_1} \int_{D}^{+\infty} dz_{fs_1} u(r_{fs_1}) + \frac{\beta^2}{2} M V_s^{M-1} \times \Bigg[\int_{-\infty}^{+\infty} dx_{fs_1} \int_{-\infty}^{+\infty} dy_{fs_1} \int_{D}^{+\infty} dz_{fs_1} u^2(r_{fs_1}) + \frac{M-1}{V_s} \int_{-\infty}^{+\infty} dx_{fs_1} \int_{-\infty}^{+\infty} dy_{fs_1} \int_{D}^{+\infty} dz_{fs_1} \times \int_{-\infty}^{+\infty} dx_{fs_2} \int_{-\infty}^{+\infty} dy_{fs_2} \int_{D}^{+\infty} dz_{fs_2} u(r_{fs_1}) u(r_{fs_2})\Bigg] + \mathscr{O}(u^3)\Bigg\}, \quad (16)$$

or, by rearranging the expression,

$$\exp\left(-\frac{w(D)}{k_B T}\right) = F_s(T) V_s^M \times \Bigg\{1 - \beta\rho_s \int_{-\infty}^{+\infty} dx_{fs_1} \int_{-\infty}^{+\infty} dy_{fs_1} \int_{D}^{+\infty} dz_{fs_1} u(r_{fs_1}) + \frac{\beta^2}{2}\rho_s \times \Bigg[\int_{-\infty}^{+\infty} dx_{fs_1} \int_{-\infty}^{+\infty} dy_{fs_1} \int_{D}^{+\infty} dz_{fs_1} u^2(r_{fs_1}) + \frac{M-1}{V_s} \int_{-\infty}^{+\infty} dx_{fs_1} \int_{-\infty}^{+\infty} dy_{fs_1} \int_{D}^{+\infty} dz_{fs_1} \times \int_{-\infty}^{+\infty} dx_{fs_2} \int_{-\infty}^{+\infty} dy_{fs_2} \int_{D}^{+\infty} dz_{fs_2} u(r_{fs_1}) u(r_{fs_2})\Bigg] + \mathscr{O}(u^3)\Bigg\}. \quad (17)$$

For convenience Equation (17) can be given in compact form in terms of the average of the configurational energy and the square of the energy as

$$\exp\left(-\frac{w(D)}{k_B T}\right) = F_s(T) V_s^M \left[1 - \beta\langle U\rangle + \frac{\beta^2}{2}\langle U^2\rangle + \mathscr{O}(U^3)\right], \quad (18)$$

where

$$\langle U\rangle = \rho_s \int_{-\infty}^{+\infty} dx_{fs_1} \int_{-\infty}^{+\infty} dy_{fs_1} \int_{D}^{+\infty} dz_{fs_1} u(r_{fs_1}), \quad (19)$$

and

$$\langle U^2\rangle = \rho_s \Bigg[\int_{-\infty}^{+\infty} dx_{fs_1} \int_{-\infty}^{+\infty} dy_{fs_1} \int_{D}^{+\infty} dz_{fs_1} u(r_{fs_1})^2 + \frac{M-1}{V_s} \int_{-\infty}^{+\infty} dx_{fs_1} \int_{-\infty}^{+\infty} dy_{fs_1} \int_{D}^{+\infty} dz_{fs_1} \times \int_{-\infty}^{+\infty} dx_{fs_2} \int_{-\infty}^{+\infty} dy_{fs_2} \int_{D}^{+\infty} dz_{fs_2} u(r_{fs_1}) u(r_{fs_2})\Bigg]. \quad (20)$$

The logarithm of both sides of Equation (18) can then be taken and the right-hand side can be expanded as $\ln(1+x) = \sum_{i=1}^{\infty} {}^{(-1)^{i+1} x^i}/_{i}$ to obtain

$$w(D) = -\frac{1}{\beta}\ln\left[F_s(T) V_s^M\right] + \langle U\rangle - \frac{\beta}{2}\left[\langle U^2\rangle - \langle U\rangle^2\right] + \mathscr{O}(U^3). \quad (21)$$

It should be noted at this point that the kinetic term represented by the product of $F_s(T) V_s^M$ is solely a function of temperature for an incompressible substrate and as such does not affect the position of phase equilibria for a system in thermal equilibrium; furthermore this temperature-dependent ideal contribution can be neglected altogether if the degrees of freedom of the particles in the solid are restricted. Equation (21) can be interpreted as the high-temperature series expansion of the expression for the free-energy-averaged potential, represented by Equation (12); the latter can be rewritten for the sake of comparison as

$$w(D) = -\frac{1}{\beta}\ln\left[F_s(T) V_s^M\right] - \frac{1}{\beta}\ln\langle\exp(-\beta U)\rangle. \quad (22)$$

Even at moderate temperatures, truncation of the expansion in Equation (21) at the first term is expected to be a poor approximation of the entire series. This can be seen in Figure 3, where the free-energy-averaged (referred to as FEA hereafter) potential is compared at different levels of truncation of the expansion. The first term of the series, which represents an unweighted average of the configurational energy (UA1), clearly provides a qualitative description of the full FEA potential, but fails to reproduce the details at short distances, where presumably the roughness of the surface potential plays an important role. The incorporation of the second-order correction (UA2) over-corrects the interaction (with a divergence to negative values close to the surface), while truncating after third-order (UA3) improves the description of the potential minimum, albeit at expenses of increasing the deviation for distances close to the surface. This analysis is carried out by direct simulation of Lennard-Jones (12-6) fluid particles in the vicinity of a solid of identical Lennard-Jones (12-6) particles as will be described in the next sections. At high temperatures the higher-order terms in the expansion can be neglected, and

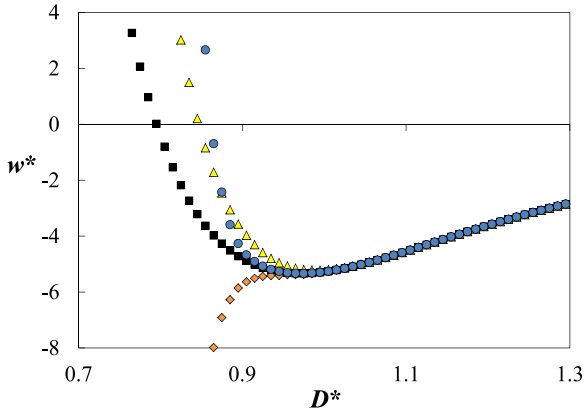

Fig. 3 Effective fluid-surface potential in reduced units ($w^* = w/\varepsilon_{\rm ff}$) as a function of reduced distance to the surface ($D^* = D/\sigma_{\rm ff}$) at a temperature $T^* = k_{\rm B}T/\varepsilon = 1$. An LJ fluid-solid interparticle interaction is considered between an LJ fluid particle and a solid of identical LJ particles ($\sigma_{\rm ff} = \sigma_{\rm ss} = \sigma_{\rm fs}$ and $\varepsilon_{\rm ff} = \varepsilon_{\rm ss} = \varepsilon_{\rm fs}$) with an exposed (111) surface. The black squares represent the corresponding effective FEA potential [i.e., considering the average of the Boltzmann factor; Equation (22) without the ideal kinetic contribution of the solid]. The colour symbols correspond to different truncations of the high-temperature expansion [Equation (21)] of the free-energy average expression. The yellow triangles correspond to the leading-order term (UA1 potential), the orange diamonds correspond to a truncation after the second-order term (UA2) and the blue circles correspond to a truncation after third-order term (UA3).

so the fluid-surface potential will be well represented by the first term in the expansion ($w \simeq \langle U \rangle$). We will now focus on this first-order term. Note that Equation (19) can be seen as a "sum" of the interactions between the fluid particle with all the particles in the solid body (where $\rho_{\rm s} {\rm d}x_{{\rm fs}_1} {\rm d}y_{{\rm fs}_1} {\rm d}z_{{\rm fs}_1}$ is the number of solid particles in a differential volume ${\rm d}x_{{\rm fs}_1} {\rm d}y_{{\rm fs}_1} {\rm d}z_{{\rm fs}_1}$). The explicit integration of $\langle U \rangle$ has been shown before (for example by Israelachvili [26] and many others) but is derived here for completeness. For an isotropic intermolecular potential, it is convenient to use cylindrical polar coordinates, which transforms Equation (19) to

$$\langle U \rangle = \rho_{\rm s} \int_D^{+\infty} {\rm d}z \int_0^{+\infty} {\rm d}R R \int_0^{2\pi} {\rm d}\theta u(\sqrt{R^2+z^2}) \quad (23)$$

As an example we take the Sutherland [64–68] potential, given by

$$u_{\rm S}(r) = \varepsilon \left(\frac{\sigma}{r}\right)^{\lambda}, \quad (24)$$

where σ is the interparticle diameter, ε is the energy well-depth and λ is the range of the intermolecular interaction, and use it to perform the integration of Equation (23) so that

$$\langle U \rangle = \rho_{\rm s} 2\pi \int_D^{+\infty} {\rm d}z \int_0^{+\infty} {\rm d}R R \varepsilon \frac{\sigma^{\lambda}}{(R^2+z^2)^{\lambda/2}}. \quad (25)$$

Here the angular integration in the plane of the surface has been carried out as the solid is assumed to be homogeneous. The result of integrating over the radial direction is given by

$$\begin{aligned} \langle U \rangle &= \rho_{\rm s} \varepsilon \sigma^{\lambda} \int_D^{+\infty} {\rm d}z \left[\frac{-1}{(\lambda-2)(R^2+z^2)^{(\lambda-2)/2}} \right]_{R=0}^{R=\infty} \\ &= \rho_{\rm s} 2\pi \varepsilon \sigma^{\lambda} \int_D^{+\infty} {\rm d}z \frac{1}{(\lambda-2) z^{(\lambda-2)}}. \end{aligned} \quad (26)$$

We refer to this intermediate integration of the intermolecular potential as the angular radial average $\phi(z,\lambda) = {}^{2\pi\varepsilon\sigma^{\lambda}}/_{(\lambda-2)z^{(\lambda-2)}}$. Equation (26) for the average potential energy can then be expressed as

$$\langle U \rangle = \rho_{\rm s} \int_D^{+\infty} {\rm d}z \phi(z,\lambda). \quad (27)$$

In the case of a solid consisting of a single uniform layer, the final integration over the normal direction would be equivalent to the incorporation of a delta function in Equation (27):

$$\langle U \rangle_{\rm l} = \rho_{\rm s_a} \int_D^{+\infty} {\rm d}z \phi(z,\lambda) \delta(z-D), \quad (28)$$

where the subscript l indicates a single layer, and the subindex a in $\rho_{\rm s_a}$ has been added to indicate that the solid density is now an area or surface density. This leads to

$$\langle U \rangle_{\rm l} = \rho_{\rm s_a} \phi(D,\lambda), \quad (29)$$

or

$$\langle U \rangle_{\rm l} = 2\pi \rho_{\rm s_a} \varepsilon \sigma^2 \frac{1}{(\lambda-2)} \left(\frac{\sigma}{D}\right)^{\lambda-2}. \quad (30)$$

It is then easy to show the expression for a generalised Lennard-Jones ($\lambda_{\rm r}$-$\lambda_{\rm a}$) potential, also known as a Mie potential [69,70], which has the form of a sum of Sutherland terms, one accounting for the repulsive and the other for the attractive contributions:

$$u_{\rm Mie}(r) = C\varepsilon \left[\left(\frac{\sigma}{r}\right)^{\lambda_{\rm r}} - \left(\frac{\sigma}{r}\right)^{\lambda_{\rm a}} \right], \quad (31)$$

where the constant

$$C = \frac{\lambda_{\rm r}}{\lambda_{\rm r}-\lambda_{\rm a}} \left(\frac{\lambda_{\rm r}}{\lambda_{\rm a}}\right)^{\frac{\lambda_{\rm a}}{(\lambda_{\rm r}-\lambda_{\rm a})}} \quad (32)$$

ensures that the potential minimum is at $-\varepsilon$, and $\lambda_{\rm r}$ and $\lambda_{\rm a}$ are the repulsive and attractive exponent, respectively. A comprehensive historical overview of the Mie potential is given in Ref. [71]. For this potential, Equation (30) has the following form

$$\langle U \rangle_{\rm l} = 2\pi \rho_{\rm s_a} C \varepsilon \sigma^2 \left[\frac{1}{(\lambda_{\rm r}-2)} \left(\frac{\sigma}{D}\right)^{\lambda_{\rm r}-2} - \frac{1}{(\lambda_{\rm a}-2)} \left(\frac{\sigma}{D}\right)^{\lambda_{\rm a}-2} \right]. \quad (33)$$

In the case of the ubiquitous Lennard-Jones (12-6) potential, Equation (33) leads to the well-known (10-4) potential:

$$\langle U\rangle_{\rm l} = 2\pi\rho_{\rm s_a}\varepsilon\sigma^2\left[\frac{2}{5}\left(\frac{\sigma}{D}\right)^{10} - \left(\frac{\sigma}{D}\right)^{4}\right]. \quad (34)$$

If however, we consider the wall to be a semi-infinite continuum, we can perform the integration implicit in Equation (26) for the Sutherland interaction, and such integration over the normal direction for an homogeneous solid density $\rho_{\rm s}$ yields

$$\begin{aligned}\langle U\rangle &= 2\pi\rho_{\rm s}\varepsilon\sigma^{\lambda}\left[\frac{-1}{(\lambda-2)(\lambda-3)(z)^{(\lambda-3)}}{\rm d}z\right]_{z=D}^{z=\infty} \\ &= 2\pi\rho_{\rm s}\frac{\varepsilon\sigma^3}{(\lambda-2)(\lambda-3)}\left(\frac{\sigma}{D}\right)^{(\lambda-3)}. \quad (35)\end{aligned}$$

As before, the development for the Mie interaction is straightforward, leading to

$$\begin{aligned}\langle U\rangle = 2\pi\rho_{\rm s_a}C\varepsilon\sigma^3\Bigg[&\frac{1}{(\lambda_{\rm r}-2)(\lambda_{\rm r}-3)}\left(\frac{\sigma}{D}\right)^{\lambda_{\rm r}-3} \\ &- \frac{1}{(\lambda_{\rm a}-2)(\lambda_{\rm a}-3)}\left(\frac{\sigma}{D}\right)^{\lambda_{\rm a}-3}\Bigg]. \quad (36)\end{aligned}$$

In the particular case of a Lennard-Jones intermolecular potential one obtains the well-known (9-3) potential

$$\langle U\rangle = 2\pi\rho_{\rm s}\varepsilon\sigma^3\left[\frac{2}{45}\left(\frac{\sigma}{D}\right)^{9} - \frac{1}{3}\left(\frac{\sigma}{D}\right)^{3}\right]. \quad (37)$$

In all of our expressions σ and ε represent the size and energy parameters of the potential of interaction between the fluid and the solid.

2.2 The (10-4-3) Steele Potential

The most widely used potential to model adsorption on carbon-based materials is (by far) the (10-4-3) potential of Steele[48,52,53]. Although it is generally applied only for graphitic structures, in the original manuscript of Steele[53] the form of the potential was also suggested as appropriate to represent the interactions of molecules with other solids involving fcc lattices with exposed (111) and (100) surfaces. Steele[52] observed that a fluid-surface potential based on sums of (10-4) potentials for the different basal planes of the solid was a better approximation than a fully integrated (9-3) potential. The expression for a sum of integrated (10-4) potentials describing the interaction with solid planes k parallel to the surface and spaced at Δ intervals is

$$\langle U\rangle = 2\pi\rho_{\rm s}\varepsilon\sigma^2\sum_{k=0}^{\infty}\left[\frac{2}{5}\left(\frac{\sigma}{D+k\Delta}\right)^{10} - \left(\frac{\sigma}{D+k\Delta}\right)^{4}\right]. \quad (38)$$

Steele[53] obtained an approximation to this potential through a particular integration of the higher contributions in the sum (other than $k=0$), where those corresponding to the D^{-10} term were neglected and those corresponding to the D^{-4} term were integrated from a chosen distance to improve the accuracy of the full potential. One can interpret[58] such an approach as an approximate representation of the solid where the first layer of atoms (the surface) is taken as an infinitely thin wall of uniform surface density. This leads to a particle-wall potential of the (10-4) form, as given by Equation (34). The rest of the solid is integrated starting from a distance $\alpha\Delta$ from the surface, to represent a slab of uniform volumetric density. In the latter integration the attractive part of the pairwise potential of the fluid-solid interaction is assumed to be predominant as is indeed the case for moderate to large distances; the repulsive part of the pair potentials active at short distances is neglected. This translates into an additional contribution to the integrated potential that is proportional to $(D+\alpha\Delta)^{-3}$. The final expression is given by[48,53]

$$\langle U\rangle = 2\pi\rho_{\rm s}\Delta\varepsilon\sigma^2\left[\frac{2}{5}\left(\frac{\sigma}{D}\right)^{10} - \left(\frac{\sigma}{D}\right)^{4} - \left(\frac{\sigma^4}{3\Delta(D+\alpha\Delta)^3}\right)\right], \quad (39)$$

where α is an adjustable parameter[72], set to $\alpha = 0.61$. The product $\rho_{\rm s}\Delta$ is the area density of the surface. The Steele (10-4-3) potential has been extended to account for polar interactions by Zhao and Johnson[59], and more recently to describe pore-like geometries by Siderius and Gelb[58].

2.3 Free-energy averaging procedure

Following Equation (12), an alternative route to the calculation of the effective FEA potential $w(D)$ is to obtain it directly from computer simulations of the explicit molecular system as an ensemble average:

$$w(D) = -\frac{1}{\beta}\ln\left\langle\exp\left(-\sum_{i=1}^{M}\beta u_{{\rm fs}_i}(x_{{\rm fs}_i}, y_{{\rm fs}_i}, z_{{\rm fs}_i})\right)\right\rangle, \quad (40)$$

where distances are expressed relative to the fluid particle, so that the minimum possible value of $z_{{\rm fs}_i}$ for any i is D ($z_{{\rm fs}_i} \geqslant D$, i.e., D is the distance from the fluid particle to the solid surface). Pairwise additivity is assumed, and the degrees of freedom of the solid particles in Equation (12) are neglected. In practice this is avoided in the simulations keeping the solid particles fixed in a lattice.

We carry out the calculation of the effective fluid-solid potentials by performing a simple Brute Force Monte Carlo simulation in the canonical (NVT) ensemble determining random positions of a single fluid particle relative to the explicit solid lattice (corresponding to different values of D). The ensemble

average is then calculated as a sum

$$w(D) = -\frac{1}{\beta}\ln\left[\frac{1}{N_{\rm cnf}}\sum_{j=1}^{N_{\rm cnf}}\exp\left(-\sum_{i=1}^{M}\beta u_{{\rm fs}_i}(x_{{\rm fs}_i},y_{{\rm fs}_i},z_{{\rm fs}_i})\right)\right], \quad (41)$$

where $N_{\rm cnf}$ is the number of unique configurations considered in the calculation of the FEA potential.

Averages are taken over at least 50 million configurations (i.e., $N_{\rm cnf} = 5\times10^7$), except for the less compact structures, for which the number of configurations is increased to 100 million (in the case of the (110) structure) and 5000 million (in the case of the (111) plane with defects). The relative positions to the surface (D) are discretised using a histogram with bins of size $0.01\sigma_{\rm ff}$, where $\sigma_{\rm ff}$ is the fluid particle diameter. At the same time the corresponding UA1 potential $\langle U\rangle$ is also calculated, for the same positions:

$$\langle U(D)\rangle = \frac{1}{N_{\rm cnf}}\sum_{j=1}^{N_{\rm cnf}}\left(\sum_{i=1}^{M}u_{{\rm fs}_i}(x_{{\rm fs}_i},y_{{\rm fs}_i},z_{{\rm fs}_i})\right). \quad (42)$$

Boundary conditions are imposed both in the x and y directions and a cutoff of $r_{\rm c} = 6\sigma_{\rm ff}$ is used for the range of the interactions (the pair-potential is simply truncated at that distance, chosen to ensure that the value of the potential is almost zero at that point). The size of the simulation box for the fcc solid is taken as 12 times the spacing between the atoms in both x and y directions and a similar length in the z direction unless a monolayered solid surface is considered, for which $z \approx 7\sigma_{\rm ff}$. In particular, the dimensions for the box when considering an fcc solid with the (111) surface exposed are $12.0\times12.124\times12.0\,\sigma_{\rm ff}^3$ (multilayered solid of 7 layers); for the box with an fcc solid with the (100) surface exposed are $12.0\times12.0\times12.0\,\sigma_{\rm ff}^3$ (multilayered solid of 9 layers), and for the box with an fcc solid with the (110) surface exposed are $12.0\times16.971\times12.0\,\sigma_{\rm ff}^3$ (multilayered solid of 12 layers). In the case of graphite the dimensions of the box are $46.731\times46.86\times40.0\,\text{Å}^3$ (solid consisting of 5 layers). The numerical values obtained for these potentials are tabulated in the supplementary material.

In order to provide a closed-analytical intermolecular potential function the resulting discrete values are also correlated by using the generic Mie form [*cf.* Equation (31)]. The corresponding Mie parameters for each of the systems studied are collected in Table 1. When the surface is less compact, such as the solids exposing (100) and (110) structures or with defects on the (111) surface layer, the Mie form does not lead to a satisfactory representation of the actual discrete potential. In such cases one can use the numerical values obtained from the simulations, and use linear interpolation to evaluate the potential.

2.4 GCMC Simulation of Adsorption

To study the effect that the use of the different averaging procedures (and corresponding potentials) has on the macroscopic adsorption isotherms we also employ the coarse-grained interactions as input for GCMC simulations in the μVT ensemble. The adsorption isotherms determined are compared with the results obtained from a detailed simulation in which all of the interactions are explicitly considered. A slit-like pore geometry is used to model the solid. Two solid blocks (each of them comprising the number of layers aforementioned) are considered, the surfaces of which are separated by a distance (in the z direction) which is slightly larger than twice the cutoff considered ($r_{\rm c} = 6.0\sigma_{\rm ff}$); for the separations and fluid densities shown the pore geometry and resulting "confinement" does not have an influence on the adsorption on a surface. The surface separation used for the adsorption in the fcc solids studied is $H = 13.0\sigma_{\rm ff}$, and that for the adsorption on graphite and graphene is $H = 12.07\sigma_{\rm ff}$. All of these distances are measured relative to the centers of the outermost solid particles. Periodic boundary conditions are imposed in the other (x and y) cartesian directions.

The only realistic system considered in our current contribution is methane adsorbed on graphite. This system is widely modelled using an LJ intermolecular potential and the Steele fluid-surface potential, and limited comparisons have been presented in the literature to evaluate the performance of alternative interaction potentials[73]. The parameters used are taken directly from Steele[53]: $\sigma_{\rm ff} = 3.81\,\text{Å}$, $\varepsilon_{\rm ff} = 148.1K$, $\sigma_{\rm ss} = 3.40\,\text{Å}$, $\varepsilon_{\rm ss} = 28.0K$, $\rho_{\rm ss} = 0.114\,\text{Å}^{-3}$ and $\Delta = 0.335\,\text{Å}$. The unlike interaction parameters are calculated using the Lorentz-Berthelot combining rules, i.e., $\sigma_{\rm fs} = (\sigma_{\rm ff}+\sigma_{\rm ss})/2$ and $\varepsilon_{\rm fs} = (\varepsilon_{\rm ff}\varepsilon_{\rm ss})^{1/2}$. In all the GCMC simulations the solid-solid interparticle interactions are neglected.

The GCMC simulations are carried out starting with an empty pore which is filled until equilibrium is attained, using a standard procedure[48,74,75]. For each Monte Carlo cycle, both the displacement of a randomly chosen fluid molecule and a random creation/destruction of a fluid molecule are attempted. Systems are left to equilibrate for at least 2 million cycles (up to 5 million are sometimes needed at the conditions of maximum coverage studied) and averages are typically taken for over a further 3 million cycles. Block averages are taken every 10000 cycles. These block averages are used to compute standard deviations to calculate the uncertainties.

In the GCMC simulations the temperature and the activity[76], directly related to the chemical potential, are specified. Simulations are also performed for bulk fluids that would hypothetically be in equilibrium with the adsorbed fluid (i.e., these are performed at the same temperature and activity) so that the density of the bulk fluid can be calculated as a simple average. This density is then used to determine the pressure at a given

temperature through the equation of state of Johnson *et al.*[77] for Lennard-Jones fluids.

3 Results and discussion

3.1 Adsorption of Methane on Graphene and Graphite

We start our analysis by studying the adsorption of methane on carbon surfaces. The choice of the system is made to assess both the adequacy of considering the solid as a continuous distribution of atoms as well as the FEA potentials. The solid is first taken as graphene; as we mentioned in the previous section we employ the specific interaction parameters of Steele[53] for methane on graphene in this case. For a solid consisting of a single layer of graphene, the integration of an intermolecular potential based on LJ interactions over such a surface leads to a (10-4) potential, as discussed earlier, *cf.* Equation (34). The corresponding (10-4) potential is compared to the effective potential obtained after summation of pair potentials between a fluid particle and every particle that forms the solid [i.e., the UA1 potential, *cf.* Equation (42)]. This comparison is plotted in Figure 4, where it can be seen that both descriptions agree quantitatively. As discussed earlier, these descriptions correspond to the use of only the leading-order term in the high-temperature expansion of the expression for the FEA potential. In order to assess the effect of temperature, the FEA potential [*cf.* Equation (41)] is depicted at relatively low temperatures in Figure 4, chosen to be $T = 59\,K$ (which in the case of the interaction potential parameters of methane corresponds to $T^* = Tk_B/\varepsilon_{ff} \approx 0.4$) and $T = 118\,\mathrm{K}$ ($T^* \approx 0.8$). Temperatures of $T^* \approx 0.4$ are below the triple point for Lennard-Jones fluids[78,79]; the behaviour of methane on carbon surfaces presents interesting phenomena at these low temperatures[80,81]. In spite of this, negligible differences are observed between the free-energy average potential and the leading-order term even at such low temperature. The GCMC simulations (not shown) also confirm that both the FEA potential and the UA1 potential lead to the same adsorption isotherms of methane on graphene; the adsorption isotherms obtained using a discrete description of the solid are also found to be essentially indistinguishable from those obtained with the coarse-grained potentials.

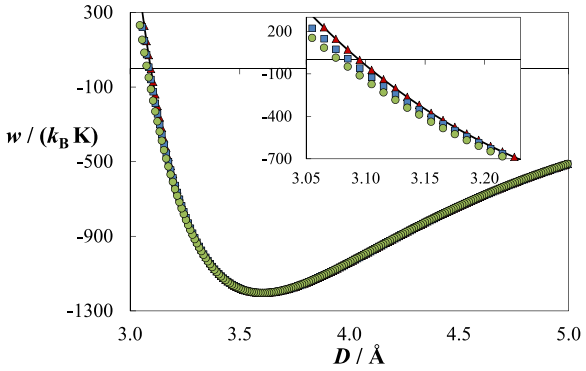

Fig. 4 Effective fluid-surface potential w as a function of distance to the surface D for the adsorption of a methane molecule on graphene. The intermolecular potential used for the explicit interactions between the fluid-solid particles of this system is the original LJ parameterization of Steele[53]: $\sigma_{ff} = 3.81\,\text{Å}$, $\varepsilon_{ff} = 148.1\,K$, $\sigma_{ss} = 3.40\,\text{Å}$ and $\varepsilon_{ss} = 28.0\,K$, with Lorentz-Berthelot combining rules for the fluid-solid interaction parameters. The symbols correspond to an effective FEA potential at a temperature $T = 59\,K$ (green circles) and $T = 118\,K$ (blue squares), and an effective UA1 potential (red triangles). The continuous curve is the corresponding (10-4) potential. An amplified view of the potential close to the wall can be seen in the inset.

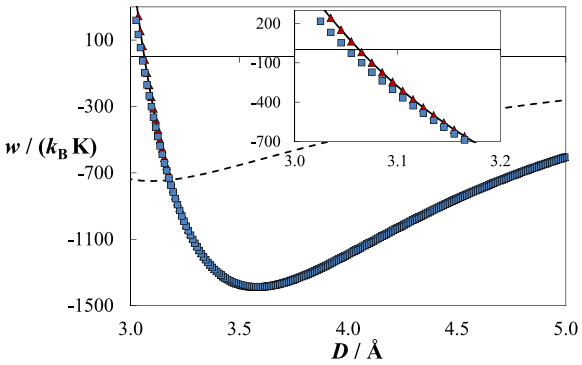

Fig. 5 Effective fluid-surface potential w as a function of distance to the surface D for the adsorption of a methane molecule on graphite. The intermolecular potential used for the explicit interactions between the fluid-solid particles of this system is the original LJ parameterization of Steele[53]: $\sigma_{ff} = 3.81\,\text{Å}$, $\varepsilon_{ff} = 148.1\,K$, $\sigma_{ss} = 3.40\,\text{Å}$ and $\varepsilon_{ss} = 28.0\,K$, with Lorentz-Berthelot combining rules for the fluid-solid interaction parameters. The symbols correspond to an effective FEA potential (blue squares) at a temperature $T = 118\,K$ and an effective UA1 potential (red triangles). The solid curve is the corresponding (10-4-3) potential. The dashed curve is the corresponding (9-3) potential. An amplified view of the potential close to the wall can be seen in the inset.

If instead one considers a graphitic structure (a multi-layer carbon), the corresponding coarse-grained integration obtained to leading-order considering it is a homogeneous material will lead to a (9-3) potential [*cf.* Equation (37)]. In Figure 5 we compare the corresponding (9-3) integrated potential with direct summation of the pair potentials of a methane molecule with every carbon atom in the solid. The integration over the parallel layers in the structure of graphite, leading to the (9-3) potential, does not even provide a qualitative description. This result is not new as it was already noted by Steele[52] and lead to the development of the (10-4-3) potential. In Figure 5 we also plot the FEA potential at a temperature of $T = 118\,\mathrm{K}$.

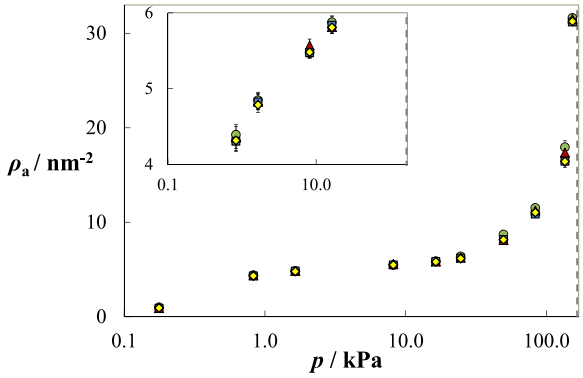

Fig. 6 Density of adsorbed methane per unit area versus pressure at a temperature T=118 K on graphite. The intermolecular potential used for the explicit interactions between the fluid-fluid and fluid-solid particles of this system is the original LJ parameterization of Steele[53]: $\sigma_{ff} = 3.81$ Å, $\varepsilon_{ff} = 148.1K$, $\sigma_{ss} = 3.40$ Å and $\varepsilon_{ss} = 28.0K$, with Lorentz-Berthelot combining rules for the fluid-solid interaction parameters. The symbols correspond to the results from GCMC simulations for the discrete solid (yellow diamonds), for a fluid-wall interaction represented by the effective FEA potential (blue squares), for a fluid-wall interaction represented by the effective UA1 potential (red triangles) and for a fluid-wall interaction represented by the (10-4-3) Steele potential (green circles). The dashed line (to the right of the diagram) is the corresponding saturation pressure of the bulk fluid at this temperature. An amplified view of the low-pressure area can be seen in the inset.

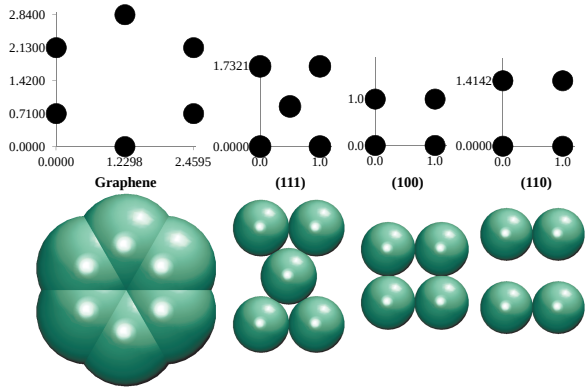

Fig. 7 Schematic comparing the packing in the hexagonal basal planes of graphite (or graphene), as well as the (111), (100) and (110) crystallographic planes studied in this work. The particles are depicted at the relative positions (top plots) and with the equivalent diameters (bottom plots) used in the simulations.

As before, we can see that the FEA potential differs only slightly from the leading-order term descriptions of the expansion. One observes the most important deviations close to the surface of the solid, a region of relevance to the adsorption. In practice, the various coarse-graining approaches provide an equivalent representation of the adsorption in this case, as confirmed in the calculation of the adsorption isotherms, shown in Figure 6. The shape of the adsorption isotherm conforms to the sigmoid isotherm corresponding to type II in the BET classification[82]. At low vapour pressures the density of the adsorbed fluid raises at a considerable rate, which indicates that the adsorbate-adsorbent interaction is dominant with respect to the forces between the adsorbate molecules. At pressures close to the vapour pressure of the bulk fluid, the density of adsorbed fluid increases steeply towards the corresponding density of the bulk phase, which is an artifact of the confinement geometry. As seen the different effective potentials also provide a good description of the adsorption when compared with the exact result obtained by calculating the solid-fluid potential explicitly (*cf.* Figure 6).

In the honeycomb lattices that form the layers of graphitic carbons the space between adjacent carbons is only 1.42 Å as compared to the characteristic diameter, 3.4 Å, hence the surface layers are tightly packed (*cf.* Figure 7). Furthermore, the size of a methane molecule (3.82 Å) is relatively large in comparison. As a result, the molecule does not feel the heterogeneity of the surface which is presumably the main reason for the similarity between the different averaging scenarios.

3.2 Effect of surface layer corrugation

The adequacy of the various coarse-graining methodologies in describing the effects of the geometric surface heterogeneity on adsorption is studied in this section for simple model systems. An LJ adsorbent fluid interacting with an LJ multilayered solid adsorbate of otherwise identical particles ($\sigma_{ff} = \sigma_{ss} = \sigma_{fs}$ and $\varepsilon_{ff} = \varepsilon_{ss} = \varepsilon_{fs}$) arranged in the form of a closed-packed fcc structure ($\rho_s\sigma^3 = \sqrt{2}$) is considered. Three different possible orientations are selected for the solid, so that the face exposed to the fluid is based on the (111), (100), or (110) lattice plane (see Figure 7). It is apparent (and perhaps rather striking) how rough these surfaces are as compared to the hexagonal base plane of graphitic carbon. Higher deviations between a simple unweighted average of pair-potential sums and a free-energy averaged potential are to be expected at low temperature for these faces of the fcc structure. We start with the case in which the solid face is based on a single surface monolayer. A comparison between these effective potentials can be seen in Figure 8 at a reduced temperature of the Lennard-Jones fluid of $T^* = 1$ for the three different monolayer solids considered. One can see from Figure 9 that in all three cases the adsorption isotherms observed corresponds to Type III[82]. The fluid adsorbed per unit area increases with pressure until the vapour pressure of the fluid at the corresponding temperature is reached (which is the saturation value). At low pressure the amount adsorbed is negli-

gible; it increases suddenly at pressures near saturation, giving an indication of the dominant forces between adsorbate molecules over the adsorbate-adsorbent interaction. It is seen that a consideration of the FEA potential leads to softer effective potentials, compared to the simple unweighted energy average, with an attractive range spanning to distances closer to the wall. This softening of the potential is strongly dependent on the corrugation of the surface and indicates that the averaging technique is taking into account the effect of the fluid particles exploring the gaps of the surface at low temperature. This effect is not captured when one considers only an unweighted average of the configurational energy (either based on sums or integration). Although for the sake of clarity this has been omitted from Figure 8, an integration over the structureless surface (i.e., the (10-4) potential) provides essentially the same description as the unweighted average of the pair-potential sums for all three surface geometries. Comparing the deviations between the effective potentials for the different solid orientations we can see that in general the FEA fluid-surface potential deviates more from the (10-4) potential as the surface structure becomes less dense.

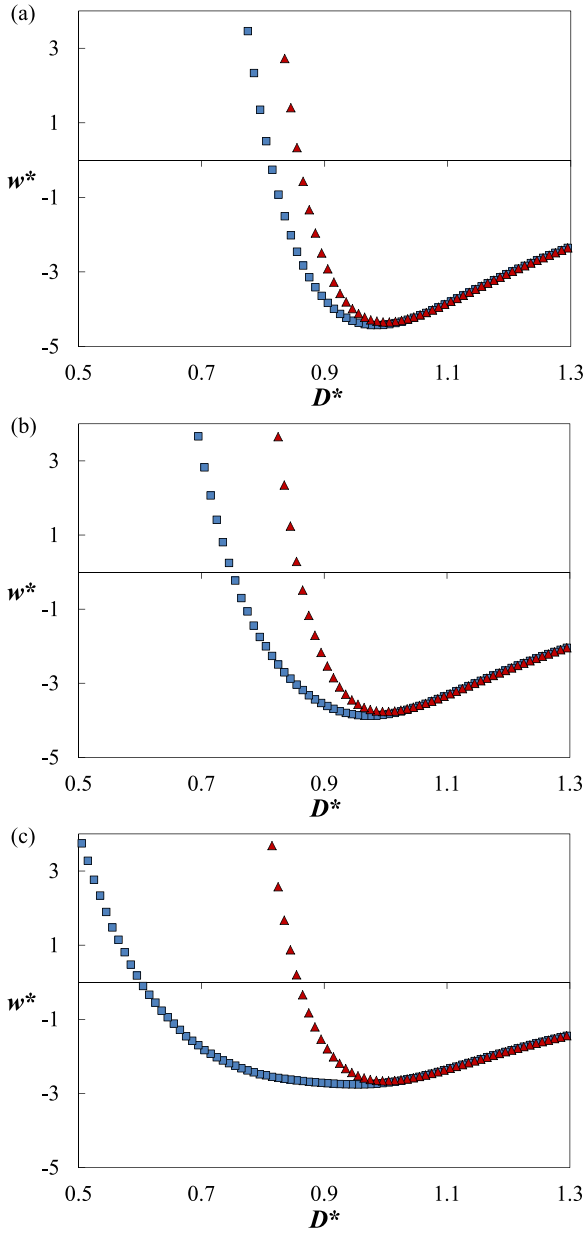

Fig. 8 Effective fluid-surface potentials in reduced units ($w^* = w/\varepsilon_{ff}$) as a function of reduced distance to the surface ($D^* = D/\sigma_{ff}$). An LJ fluid-solid interparticle interaction is considered between an LJ adsorbent fluid particle and a single monolayer solid adsorbate surface of identical LJ particles ($\sigma_{ff} = \sigma_{ss} = \sigma_{fs}$ and $\varepsilon_{ff} = \varepsilon_{ss} = \varepsilon_{fs}$) with (a) (111), (b) (100) and (c) (110) geometries. The blue squares represent the corresponding effective FEA potential at a temperature $T^* = k_B T/\varepsilon_{ff} = 1$ and the red triangles the corresponding effective UA1 potential.

The deviation between these effective potentials is further assessed in the description of an adsorption isotherm at $T^* = 1$ of an LJ adsorbent fluid on an LJ monolayer solid adsorbate. These are compared in Figure 9 with the corresponding isotherm obtained for a discrete description of the solid. In the case of a (111) solid monolayer [Figure 9(a)], both FEA and UA1 potentials provide a good approximation of the adsorption obtained with the discrete description, the deviations falling within (or close to) the standard deviation of the simulation results. The use of an UA1 potential appears to result in a systematic underprediction of the density of adsorbed fluid particles at this temperature, which is a direct consequence of the shorter attractive range with the wall. The underestimation of the density of adsorbed fluid particles resulting from the use of the temperature-independent unweighted average is more pronounced in the case of the (100) and (110) monolayer solids [Figure 9(b) and (c)], as would be expected on the basis of the increased softness of the free-energy averaged potential at shorter distances compared to the unweighted potential. The use of a free-energy averaged potential is clearly a requirement in the case of the (110) surface, the most corrugated of all the surfaces we have studied.

In the case of a solid formed from multiple layers in an fcc structure, the trends in results obtained are very similar and to avoid redundancy we limit the discussion to a comparison of the two effective potentials used to model an fcc solid with an exposed (110) surface, depicted in Figure 10 at a reduced temperature of $T^* = 1$. The corresponding results for the adsorption isotherms obtained from the GCMC simulations are given in Figure 11.

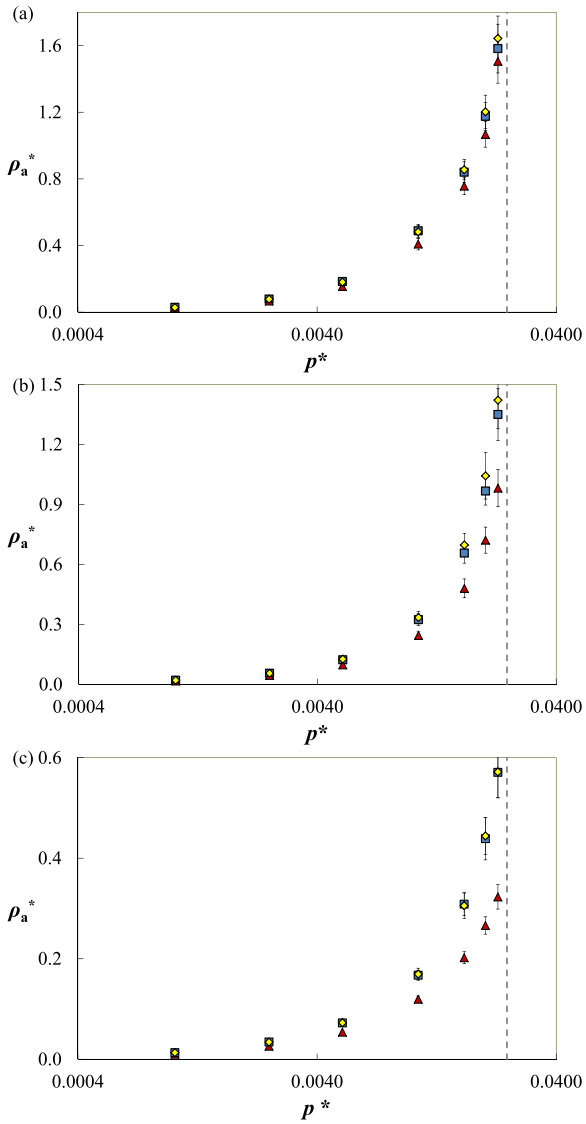

Fig. 9 Reduced density of adsorbed LJ fluid per unit area ($\rho_a^* = \rho_a \sigma_{ff}^2$) versus reduced pressure ($p^* = p\sigma^3/\varepsilon_{ff}$) at reduced temperature $T^* = k_B T/\varepsilon_{ff} = 1$. An LJ adsorbent fluid interacting with a single monolayer solid adsorbate surface of identical LJ particles ($\sigma_{ff} = \sigma_{ss} = \sigma_{fs}$ and $\varepsilon_{ff} = \varepsilon_{ss} = \varepsilon_{fs}$) with (a) (111), (b) (100) and (c) (110) geometries is considered. The symbols correspond to the results from GCMC simulations for the discrete solid description (yellow diamonds), for a fluid-wall interaction represented by the corresponding effective FEA potential (blue squares) and for a fluid-wall interaction represented by the corresponding effective UA1 potential (red triangles). The dashed line is the corresponding saturation pressure of the bulk fluid at this temperature.

3.3 Heterogeneous surfaces

The coarse graining of potentials is of course most useful for surfaces that possess either structural or energetic heterogeneities. Solids of practical interest invariably contain these types of heterogeneities and the assumption of a perfect crys-

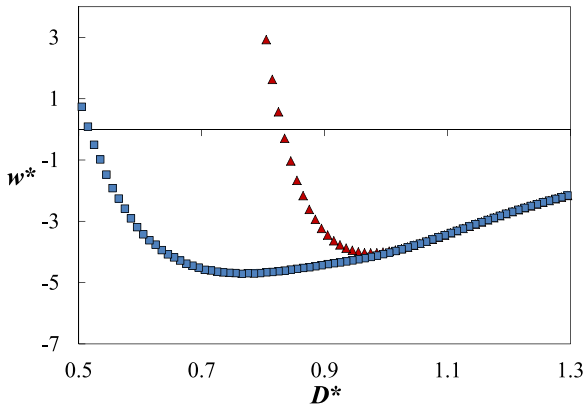

Fig. 10 Effective fluid-surface potentials in reduced units ($w^* = w/\varepsilon_{ff}$) as a function of reduced distance to the surface ($D^* = D/\sigma_{ff}$). An LJ fluid-solid interparticle interaction is considered between an LJ adsorbent fluid particle and an fcc solid adsorbate of identical LJ particles ($\sigma_{ff} = \sigma_{ss} = \sigma_{fs}$ and $\varepsilon_{ff} = \varepsilon_{ss} = \varepsilon_{fs}$) exposing a (110) surface. The blue squares represent the corresponding effective FEA potential at a temperature $T^* = k_B T/\varepsilon_{ff} = 1$ and the red triangles the corresponding effective UA1 potential.

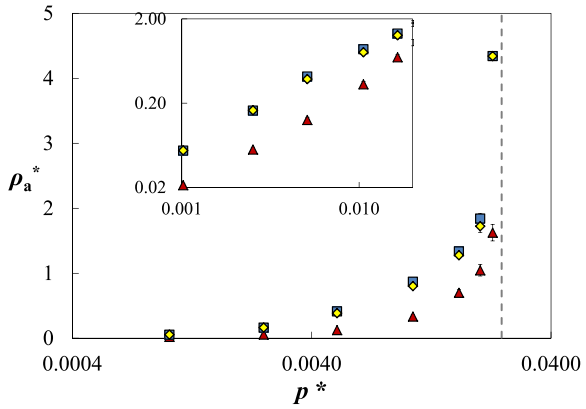

Fig. 11 Reduced density of adsorbed LJ fluid per unit area ($\rho_a^* = \rho_a \sigma_{ff}^2$) versus reduced pressure ($p^* = p\sigma^3/\varepsilon_{ff}$) at reduced temperature $T^* = k_B T/\varepsilon_{ff} = 1$. An LJ adsorbent fluid interacting with an fcc solid adsorbate of identical LJ particles ($\sigma_{ff} = \sigma_{ss} = \sigma_{fs}$ and $\varepsilon_{ff} = \varepsilon_{ss} = \varepsilon_{fs}$) exposing a (110) surface is considered. The symbols correspond to the results from GCMC simulations for the discrete solid description (yellow diamonds), for a fluid-wall interaction represented by the corresponding FEA potential (blue squares) and for a fluid-wall interaction represented by the corresponding UA1 potential (red triangles). The dashed line is the corresponding saturation pressure of the bulk fluid at this temperature. An amplified view of the low pressure area can be seen in the inset.

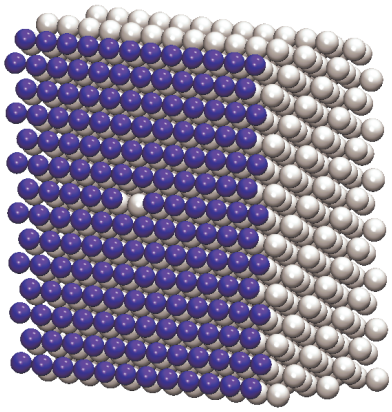

Fig. 12 Representation of the solid with a vacancy on a (111) surface. The LJ surface particles are represented by the blue coloured spheres; the particles in grey represent identical LJ particles below the first layer of the solid.

talline structure may be a gross oversimplification[83]. The accuracy of the effective potentials is first assessed in the study of a solid with a (111) surface containing a single defect within the simulation box. The surface studied thus corresponds to a vacancy per 168 particles of the original surface, as shown in Figure 12. The changes in the shape of the fluid-surface potential caused by the addition of this apparently small heterogeneity are shown in Figure 13, where the potential is compared to that of the perfect crystalline solid (without defects). It can be seen that the introduction of even a small defect concentration leads to a marked influence on the effective FEA potential. This potential now presents a second minimum at very short range. If the free-energy expansion of the potential is truncated at first order it can be seen that the vacancy has a negligible effect on the shape of the potential, indicating that at high temperature the fluid particles do not sample the defect on the surface to any discernible degree. The inclusion of further defects produces an increase in the depth of the first minimum while decreasing that of the second.

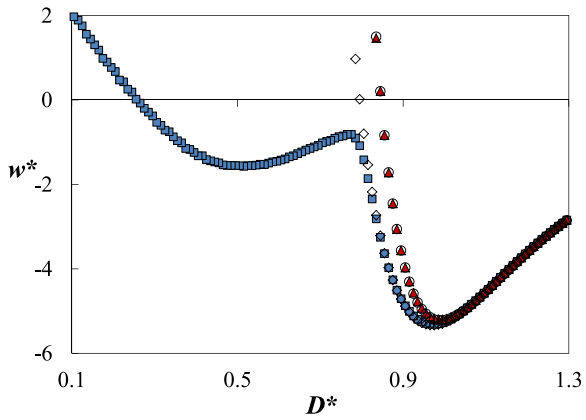

Fig. 13 Effective fluid-surface potentials in reduced units ($w^* = w/\varepsilon_{\rm ff}$) as a function of reduced distance to the surface ($D^* = D/\sigma_{\rm ff}$). An LJ fluid-solid interparticle interaction is considered between an LJ adsorbent fluid particle and an fcc solid adsorbate of identical LJ particles ($\sigma_{\rm ff} = \sigma_{\rm ss} = \sigma_{\rm fs}$ and $\varepsilon_{\rm ff} = \varepsilon_{\rm ss} = \varepsilon_{\rm fs}$) exposing a (111) surface with a single vacancy. The solid symbols represent the corresponding effective FEA potential (blue squares) at a temperature $T^* = k_{\rm B}T/\varepsilon_{\rm ff} = 1$ and the corresponding effective UA1 potential (red triangles). For purposes of comparison the open symbols correspond to the effective FEA potential (diamonds) at a temperature $T^* = k_{\rm B}T/\varepsilon_{\rm ff} = 1$ and the effective UA1 potential (circles) for the case of a perfect crystalline solid exposing a (111) surface.

Both average free-energy and unweighted-configurational-energy potentials are used to determine adsorption isotherms and the results are compared to those obtained for the discrete solid in Figure 14. At low pressure the adsorption obtained with the FEA potential agrees fairly well with that obtained using the explicit atomic description, while the potential based on the leading-order truncation is seen to lead to an underestimation of the amount of fluid adsorbed. At higher pressure, positions closer to the wall are favoured in the case of the system with the FEA potential. The latter implicitly takes into account the energetic bias of a particle being close to the vacancy compared to being at other positions. The result is a slight overestimation of the density of adsorbed fluid at pressures close to saturation, in comparison to the results obtained with the explicit description of the solid. This is of course a direct consequence of the way the free-energy average is computed, taking into account only the Henry's low-density limit, i.e., the interaction of a single fluid particle with the wall. Fluid-fluid interactions are assumed to be independent of the adsorption, while for filled pores or densely packed surface layers clearly cooperative effects will come into play[84].

Finally we study the case of a solid with chemical periodicities on its surface represented by heterogeneous energetics. In particular we consider a surface with alternating strips of solid particles characterised by different interaction energies: $\varepsilon_{\rm ss}$ (i.e., identical to that of the fluid and the rest of the solid particles) in one stripe and $2 \times \varepsilon_{\rm ss}$ in the other stripe; all the other fluid-solid interactions are otherwise identical, and Lorentz-Berthelot combining rules are used to obtain the fluid-solid interaction parameters. For this study we examine an fcc solid with a (110) surface. The arrangement of the stripes is represented in Figure 15. The coarse-grained potentials for the fluid-solid interaction are plotted in Figure 16. As expected, adding these energetic heterogeneities on the surface results in overall potentials with a deeper minimum, compared to the perfectly homogeneous surfaces. We can also see that the increase in the depth of the potential is more pronounced in the case of the FEA potential, compared to the simple UA1.

The performance of these effective potentials is compared in the computation of an adsorption isotherm in Figure 17. We can see that in spite of incorporating a large range of chemical heterogeneity, the FEA potential provides a good representation of the adsorption isotherm determined with a explicit atomistic description, while the use of a simple UA1 potential leads to a considerable underprediction of the adsorbed fluid density.

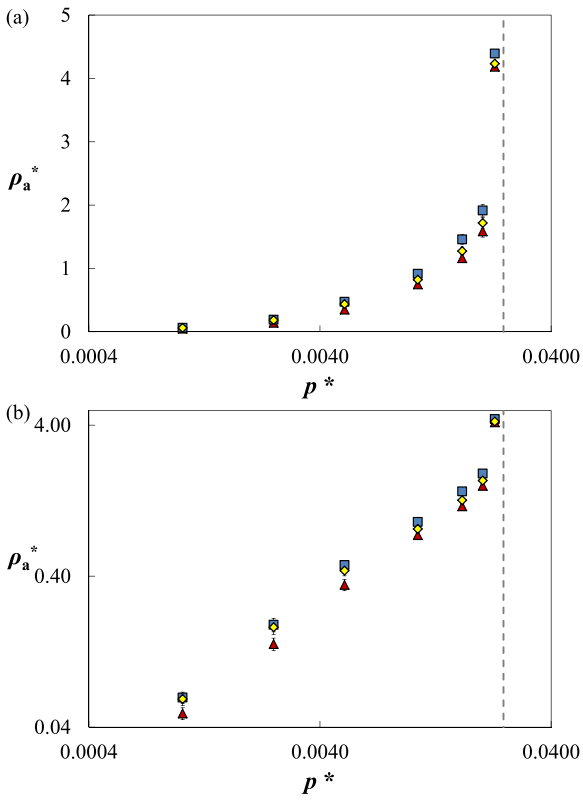

Fig. 14 Reduced density of adsorbed LJ fluid per unit area ($\rho_a^* = \rho_a \sigma_{ff}^2$) versus reduced pressure ($p^* = p\sigma^3/\varepsilon_{ff}$) at reduced temperature $T^* = k_B T/\varepsilon_{ff} = 1$. An LJ adsorbent fluid interacting with an fcc solid adsorbate of identical LJ particles ($\sigma_{ff} = \sigma_{ss} = \sigma_{fs}$ and $\varepsilon_{ff} = \varepsilon_{ss} = \varepsilon_{fs}$) exposing a (111) surface with a vacancy is considered. The difference between figures (a) and (b) is the logarithmic scale in densities. The symbols correspond to the results from GCMC simulations for a discrete solid description (yellow diamonds), for a fluid-wall interaction represented by the corresponding FEA potential (blue squares) and for a fluid-wall interaction represented by the corresponding UA1 potential (red triangles). The dashed line is the corresponding saturation pressure of the bulk fluid at this temperature.

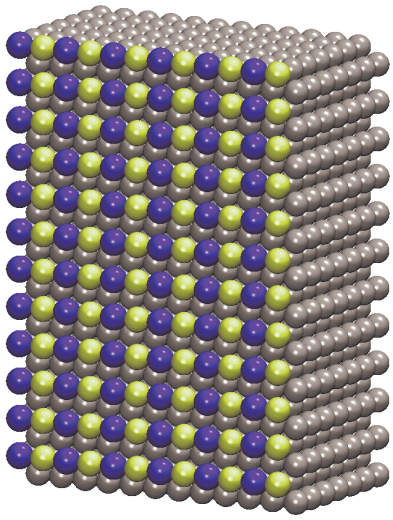

Fig. 15 Representation of the solid with energetic heterogeneities on a (110) surface. The particles comprising the main body of the solid (represented in grey to emphasise the surface) are identical to those of the fluid ($\sigma_{ff} = \sigma_{ss} = \sigma_{fs}$ and $\varepsilon_{ff} = \varepsilon_{ss} = \varepsilon_{fs}$), and identical to the blue spheres, whereas the interaction parameters characterising the yellow spheres are σ_{ss} and $2 \times \varepsilon_{ss}$ (and therefore $\sigma_{fs} = \sigma_{ss}$ and $\varepsilon_{fs} = \sqrt{2} \times \varepsilon_{ss}$).

4 Conclusions

Obtaining realistic effective fluid-surface potentials is an essential step in the development of theories of adsorption on solid substrates. Fluid-surface potentials are commonly developed based on unweighted averages of the sum of the intermolecular potential of a fluid molecule with the atoms that constitute the solid. Assuming that the solid is homogeneous and the pairwise interactions follow a Lennard-Jones (12-6) model, this leads to integrated potentials such as the commonly used (9-3) and (10-4) formulations. As an alternative, we provide a detailed analysis of the use of free-energy-averaged (FEA) potentials to study surface adsorption. The expression to obtain these potentials is developed here and the resulting forms are compared to the potentials based on unweighted-averages of the configurational energy (UA1). The latter are shown to be equivalent to the leading-order term in the high-temperature expansion represented by the FEA potential. An examination of the FEA potential makes clear that the effective coarse-grained fluid-surface potentials should be temperature dependent, while this temperature dependence is neglected if the (10-4), (9-3) or (10-4-3) potentials or their equivalents are used. Both types of averages (weighted and unweighted) converge to the same interaction at high temperatures, where the intricate details of the surface are smeared out.

We have evaluated the use of both UA1 and FEA potentials

for various types of fluid-solid interactions and we have used them to describe adsorption isotherms by undertaking GCMC simulations. In particular we have studied the interaction and adsorption of methane on graphene and graphite, as well as the corresponding behaviour of the prototypical LJ fluid adsorbent on different faces of fcc LJ solids adsorbates. The FEA potentials are found to provide a more accurate representation of the fluid-solid interaction. FEA potentials can also be used to take into account the fact that fluid particles are prone to explore the gaps of the surface at temperatures where the kinetic energy is not dominant, which is reflected by softer effective potentials as compared to the corresponding UA1 potential. The less compact and corrugated the surface is, the less accurate unweighted averages are found to be compared with the FEA potentials.

We conclude that the use of an UA1 or an analytical integration such as the (10-4) potential should be restricted to high temperatures. This also applies to the (10-4-3) potential for fcc solids. For very compacted (or less corrugated) surfaces such as that of graphene (or graphite), the use of a (10-4) [or a (10-4-3)] potential will lead to negligible deviations, and therefore it is a good approximation even at the lowest temperatures. Presumably the excellent agreement rendered by the (10-4-3) potential for graphitic substrates even at low temperature may be the reason why FEA potentials are not in wider use. However, the wider the lattice spacings in comparison to the molecular diameter of the fluid, the more significant the deviations of a type (10-4-3) potential are expected to be from a fully atomistic description. In all cases using a FEA potential to simplify the fluid-solid by a fluid-wall interaction

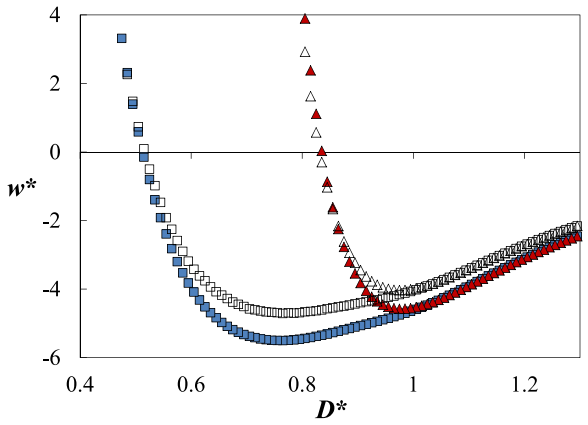

Fig. 16 Effective fluid-surface potentials in reduced units ($w^* = w/\varepsilon_{ff}$) as a function of reduced distance to the surface ($D^* = D/\sigma_{ff}$). An LJ fluid-solid interparticle interaction is considered between an LJ adsorbent fluid particle and an fcc solid adsorbate exposing a (110) surface with energetic heterogeneities comprising alternating stripes of solid particles of different interaction energy; one of the stripes is characterised by particles identical to those of the fluid and the main body of the solid ($\sigma_{ff} = \sigma_{ss} = \sigma_{fs}$ and $\varepsilon_{ff} = \varepsilon_{ss} = \varepsilon_{fs}$), whereas the other stripe is characterised by the interaction parameters σ_{ss} and $2 \times \varepsilon_{ss}$ (and therefore $\sigma_{fs} = \sigma_{ss}$ and $\varepsilon_{fs} = \sqrt{2} \times \varepsilon_{ss}$). The solid symbols represent the corresponding effective FEA potential (blue squares) at a temperature $T^* = k_B T/\varepsilon_{ff} = 1$ and the corresponding UA1 potential (red triangles). For purposes of comparison the open symbols correspond to the effective FEA potential (diamonds) at a temperature $T^* = k_B T/\varepsilon_{ff} = 1$ and the effective UA1 potential (circles) for the case of a perfect crystalline solid exposing a (110) surface.

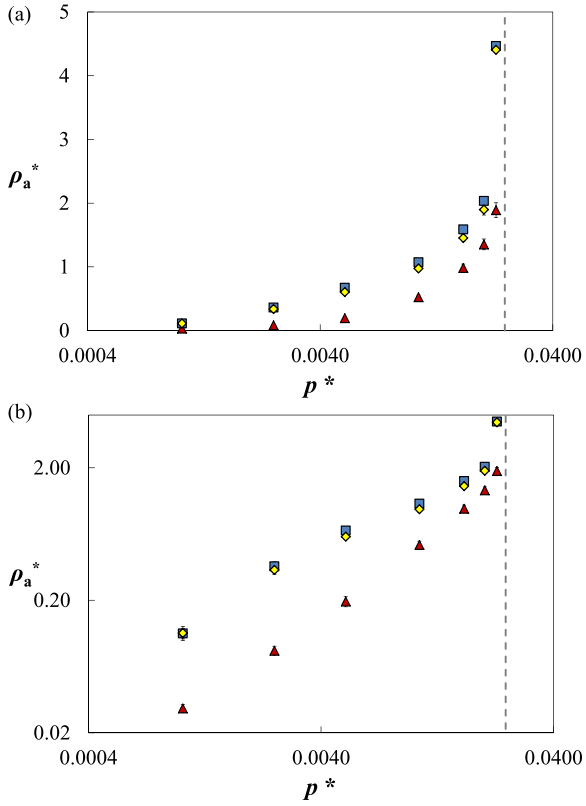

Fig. 17 Reduced density of adsorbed LJ fluid per unit area ($\rho_a^* = \rho_a \sigma_{ff}^2$) versus reduced pressure ($p^* = p\sigma^3/\varepsilon_{ff}$) at reduced temperature $T^* = k_B T/\varepsilon_{ff} = 1$. An LJ adsorbent fluid interacting with an fcc solid adsorbate exposing a (110) surface with energetic heterogeneities in alternating stripes is considered; one of the stripes is characterised by particles identical to those of the fluid and the main body of the solid ($\sigma_{ff} = \sigma_{ss} = \sigma_{fs}$ and $\varepsilon_{ff} = \varepsilon_{ss} = \varepsilon_{fs}$), whereas the other stripe is characterised by the interaction parameters σ_{ss} and $2 \times \varepsilon_{ss}$ (and therefore $\sigma_{fs} = \sigma_{ss}$ and $\varepsilon_{fs} = \sqrt{2} \times \varepsilon_{ss}$). The difference between figures (a) and (b) is the logarithmic scale in densities. The symbols correspond to the results from GCMC simulations for a discrete solid description (yellow diamonds), for a fluid-wall represented by the corresponding effective FEA potential (blue squares) and for a fluid-wall represented by the corresponding UA1 potential (red triangles). The dashed line is the corresponding saturation pressure of the bulk fluid at this temperature.

has shown to be a reliable approach for the representation of the adsorption behaviour of explicit atomistic systems, and a generalisation of conventional methods. For solids with defects there will be a point at which the representation of the solid by a continuum wall will not be a good approximation. When the solid contains vacancies, FEA potentials may lead to an over weighting of those positions therefore leading to an overestimation of the fluid-solid interaction. Solids containing chemical periodicities embodied through energetic heterogeneities are however better represented, even for highly heterogeneous systems, where FEA potentials provide an excellent agreement with the adsorption isotherm determined from the explicit atomistic potentials. At high temperatures the fluid particles do not feel the latter types of heterogeneities on the surface to the same extent, and as a consequence simple UA1 potentials lead to undepredictions of adsorption apart from at high temperature.

In conclusion, we have shown that the use of free-energy averages is a promising approach to the accurate coarse graining of detailed atomistic potentials. Incorporating average free-energy potentials, and thereby considering their appropriate temperature dependence, should aid in improving the theoretical basis of surface adsorption theories. Temperature-independent average potentials such as the (10-4-3) potential are also commonly employed in classical density functional theories (DFTs)[85] of surface adsorption and confined systems[6,47,86]. As a consequence the DFT calculations will suffer from the same deficiencies (as discussed for the simulation studies) because unweighted average surface potentials of this type do not generally provide a good representation of the effective substrate-fluid interactions apart from in the high-temperature limit. The use of free-energy average interactions such as the FEA potentials described in our current manuscript would therefore also be highly desirable in any DFT description of adsorption. In future work we intend to extend recent work on the coarse-graining of molecular fluids with the Mie potential[87–91] to include a consideration of surface adsorption, making use of group-contribution versions of the theory[92] to aid in the prediction of the fluid-solid interaction.

5 Acknowledgements

The authors acknowledge generous funding from the U.K. Engineering and Physical Sciences Research Council (EPSRC) through grants (EP/E016340, EP/I018212, EP/J010502 and EP/J014958). We would like to acknowledge that the QCCSRC is funded jointly by Qatar Petroleum, Shell, and the Qatar Science & Technology Park.

References

1 M. Polanyi, *Verh. Deut. Phys. Ges.*, 1914, **16**, 1012.
2 M. Polanyi, *Verh. Deut. Phys. Ges.*, 1916, **18**, 55–80.
3 I. Langmuir, *J. Am. Chem. Soc.*, 1918, **40**, 1361–1403.
4 S. Brunauer, *The adsorption of gases and vapors (Volume I, Physical Adsorption)*, Oxford University Press, London, 1945.
5 W. Rudzinski and D. H. Everett, *Adsorption of Gases on Heterogeneous Surfaces*, Academic Press Ltd, London, 1992.
6 A. Dabrowski, *Adv. Colloid Interface Sci.*, 2001, **93**, 135 – 224.
7 K. Y. Foo and B. H. Hameed, *Chem. Eng. J.*, 2010, **156**, 2 – 10.
8 Z. Cao, J. W. Tester, K. A. Sparks and B. L. Trout, *J. Phys. Chem. B*, 2001, **105**, 10950–10960.
9 T. S. Jakubov and D. E. Mainwaring, *J. Colloid Interf. Sci.*, 2002, **252**, 263–268.
10 L. Zhan, K. X. Li, R. Zhang, Q. F. Liu, C. X. L and L. C. Ling, *J. Supercrit. Fluids*, 2004, **28**, 37 – 45.
11 A. M. Czerny, P. Bénard and R. Chahine, *Langmuir*, 2005, **21**, 2871–2875.
12 M. Castro, R. Martinez, A. Martinez and H. C. Rosu, *Physica A*, 2010, **389**, 3140 – 3148.
13 M. Castro, H. C. Rosu and A. Martinez, *J. Chem. Eng. Data*, 2012, **57**, 1875–1880.
14 S. Dufal, A. Galindo, G. Jackson and A. J. Haslam, *Mol. Phys.*, 2012, **110**, 1223–1240.
15 E. Dundar, R. Zacharia, R. Chahine and P. Bnard, *Int. J. Hydrogen Energ.*, 2012, **37**, 9137 – 9147.
16 M. G. Bjørner, A. A. Shapiro and G. M. Kontogeorgis, *Ind. Eng. Chem. Res.*, 2013, **52**, 2672–2684.
17 L. Onsager, *Chem. Rev.*, 1933, **13**, 73–89.
18 G. S. Rushbrooke, *Trans. Faraday Soc.*, 1940, **36**, 1055–1062.
19 D. Cook and J. S. Rowlinson, *Proc. R. Soc. Lond., A*, 1953, **219**, 405–418.
20 J. S. Rowlinson, *Mol. Phys.*, 1958, **1**, 414–415.
21 J. W. Perram and L. R. White, *Mol. Phys.*, 1972, **24**, 1133–1142.
22 J. W. Perram and L. R. White, *Mol. Phys.*, 1974, **28**, 527–533.
23 G. Stell, J. C. Rasaiah and H. Narang, *Mol. Phys.*, 1974, **27**, 1393–1414.
24 J. S. Rowlinson, *Mol. Phys.*, 1984, **52**, 567–572.
25 A. J. Haslam, A. Galindo and G. Jackson, *Fluid Phase Equilib.*, 2008, **266**, 105–128.
26 J. N. Israelachvili, *Intermolecular and Surface Forces*, Academic Press, USA, 3rd edn, 2011.
27 W. M. Keesom, *Physik. Z.*, 1921, **22**, 129–141.
28 W. R. Smith and I. Nezbeda, in *The Reference Average Mayer-Function (RAM) Perturbation Theory for Molecular Fluids*, ed. J. M. Haile and G. A. Mansoori, American Chemical Society, Washington, D.C., 1983, ch. 12, pp. 235–279.
29 L. Verlet and J.-J. Weis, *Mol. Phys.*, 1974, **28**, 665–682.
30 O. Steinhauser and H. Bertagnolli, *Zeit. Phys. Chem.*, 1981, **124**, 33–43.
31 J. P. Hansen and I. R. McDonald, *Theory of simple liquids*, Academic Press, London, 2006, vol. 3rd ed.
32 W. L. Jorgensen and L. L. Thomas, *J. Chem. Theory Comput.*, 2008, **4**, 869–876.
33 S. Zhou and J. R. Solana, *Chem. Rev.*, 2009, **109**, 2829–2858.
34 K. E. Gubbins, *Mol. Phys.*, 2013, **111**, 1–32.
35 R. W. Zwanzig, *J. Chem. Phys.*, 1954, **22**, 1420–1426.
36 R. Z. Peierls, *Z. Phys.*, 1933, **80**, 763–791.
37 R. Z. Peierls, *Selected Scientific Papers of Sir Rudolf Peierls: With Commentary (Series in 20th Century Physics)*, World Scientific Publishing, Singapore, 1997.
38 J. A. Pople, *Proc. R. Soc. Lond. A*, 1952, **215**, 67–83.
39 J. A. Barker, *Proc. R. Soc. Lond. A*, 1953, **219**, 367–372.
40 I. R. McDonald, *J. Phys. C*, 1974, **7**, 1225–1236.
41 J. A. Pople, *Proc. R. Soc. Lond. A*, 1954, **221**, 498–507.
42 K. E. Gubbins and C. H. Twu, *Chem. Eng. Sci.*, 1978, **33**, 863–878.

43 C. N. Likos, *Phys. Rep.*, 2001, **348**, 267 – 439.
44 S. Izvekov and G. A. Voth, *J. Phys. Chem. B*, 2005, **109**, 2469–2473.
45 R. Faller, *Phys. Chem. Chem. Phys.*, 2009, **11**, 1867–1868.
46 *Coarse-Graining of Condensed Phase and Biomolecular Systems*, ed. G. A. Voth, CRC Press / Taylor and Francis, Boca Raton, FL, 2009.
47 L. D. Gelb, K. E. Gubbins, R. Radhakrishnan and M. Sliwinska-Bartkowiak, *Rep. Prog. Phys.*, 1999, **62**, 1573.
48 D. Nicholson and N. G. Parsonage, *Computer Simulation and the Statistical Mechanics of Adsorption*, Academic Press Inc., London, 1982.
49 I. Newton, *Philosophiae Naturalis Principia Mathematica*, London, 1687, English translation of 3rd ed. by A. Motte, The Mathematical Principles of Natural Philosophy, London, 1729; Translation revised and supplied with historical and explanatory appendix by F. Cajori, University of California Press, Berkeley, 1946. Proposition XC. Problem XLIV.
50 F. London, *Z. Phys. Chem. B*, 1930, **11**, 222–251.
51 T. L. Hill, *J. Chem. Phys.*, 1948, **16**, 181–189.
52 W. A. Steele, *The Interaction of Gases with Solid Surfaces*, Pergamon, Oxford, 1974.
53 W. A. Steele, *Surf. Sci.*, 1973, **36**, 317 – 352.
54 B. K. Peterson, J. P. R. B. Walton and K. E. Gubbins, *J. Chem. Soc., Faraday Trans. 2*, 1986, **82**, 1789–1800.
55 G. J. Tjatjopoulos, D. L. Feke and J. A. Mann, *J. Phys. Chem.*, 1988, **92**, 4006–4007.
56 R. D. Kaminsky and P. A. Monson, *J. Chem. Phys.*, 1991, **95**, 2936–2948.
57 E. S. Hernandez, M. W. Cole and M. Boninsegni, *Phys. Rev. B*, 2003, **68**, 125418.
58 D. W. Siderius and L. D. Gelb, *J. Chem. Phys.*, 2011, **135**, 084703.
59 X. Zhao and J. K. Johnson, *Mol. Simulat.*, 2005, **31**, 1–10.
60 F. F. Abraham, *J. Chem. Phys.*, 1978, **68**, 3713–3716.
61 T. M. Reed and K. E. Gubbins, *Applied Statistical Mechanics*, McGraw-Hill, 1973.
62 Z. Cao, J. W. Tester and B. L. Trout, *J. Chem. Phys.*, 2001, **115**, 2550–2559.
63 G. J. Gloor, G. Jackson, F. J. Blas and E. de Miguel, *J. Chem. Phys.*, 2005, **123**, 134703.
64 W. Sutherland, *Philos. Mag.*, 1886, **22**, 81–95.
65 W. Sutherland, *Philos. Mag.*, 1887, **24**, 113–134.
66 W. Sutherland, *Philos. Mag.*, 1887, **24**, 168–187.
67 W. Sutherland, *Philos. Mag.*, 1889, **27**, 305–321.
68 W. Sutherland, *Philos. Mag.*, 1893, **36**, 507–531.
69 G. Mie, *Ann. Phys.*, 1903, **316**, 657–697.
70 E. Grüneisen, *Ann. Phys.*, 1912, **344**, 257–306.
71 T. Lafitte, A. Apostolakou, C. Avendaño, A. Galindo, C. S. Adjiman, E. A. Müller and G. Jackson, *J. Chem. Phys.*, 2013, **139**, 154504.
72 J. Stecki, *Langmuir*, 1997, **13**, 597–598.
73 M. A. Razak, D. D. Do and G. R. Birkett, *Adsorption*, 2011, **17**, 385–394.
74 M. P. Allen and D. J. Tildesley, *Computer simulation of liquids*, Clarendon Press, Oxford, 1989.
75 D. Frenkel and B. Smit, *Understanding Molecular Simulation*, Academic Press, San Diego, 2002, vol. 2nd ed.
76 E. A. Müller, *Adsorption and Phase Behaviour in Nanochannels and Nanotubes*, Springer Netherlands, 2010, pp. 41–67.
77 J. K. Johnson, E. A. Müller and K. E. Gubbins, *J. Phys. Chem.*, 1994, **98**, 6413–6419.
78 J. K. Johnson, J. A. Zollweg and K. E. Gubbins, *Mol. Phys.*, 1993, **78**, 591–618.
79 A. Ahmed and R. J. Sadus, *J. Chem. Phys.*, 2009, **131**, 174504.
80 S. Jiang, K. E. Gubbins and J. A. Zollweg, *Mol. Phys.*, 1993, **80**, 103–116.
81 S. Jiang, C. L. Rhykerd and K. E. Gubbins, *Mol. Phys.*, 1993, **79**, 373–391.
82 S. Brunauer, L. S. Deming, W. E. Deming and E. Teller, *J. Am. Chem. Soc.*, 1940, **62**, 1723–1732.
83 V. A. Bakaev and W. A. Steele, *Langmuir*, 1992, **8**, 1372–1378.
84 K. Kaneko, T. Itoh and T. Fujimori, *Chem. Lett.*, 2012, **41**, 466–475.
85 R. Evans, *Adv. Phys.*, 1979, **28**, 143–200.
86 P. I. Ravikovitch, A. Vishnyakov and A. V. Neimark, *Phys. Rev. E*, 2001, **64**, 011602.
87 C. Avendaño, T. Lafitte, A. Galindo, C. S. Adjiman, G. Jackson and E. A. Müller, *J. Phys. Chem. B*, 2011, **115**, 11154–11169.
88 T. Lafitte, C. Avendaño, V. Papaioannou, A. Galindo, C. S. Adjiman, G. Jackson and E. A. Müller, *Mol. Phys.*, 2012, **110**, 1189–1203.
89 C. Avendaño, T. Lafitte, C. S. Adjiman, A. Galindo, E. A. Müller and G. Jackson, *J. Phys. Chem. B*, 2013, **117**, 2717–2733.
90 A. Mejía, C. Herdes and E. A. Müller, *Ind. Eng. Chem. Res.*, 2014, **53**, 4131–4141.
91 E. A. Müller and G. Jackson, *Annu. Rev. Chem. Biomol.*, 2014, **5**, 405–427.
92 V. Papaioannou, T. Lafitte, C. Avendaño, C. S. Adjiman, G. Jackson, E. A. Müller and A. Galindo, *J. Chem. Phys.*, 2014, **140**, 154102.

Table 1 Parameters † obtained through correlation of the corresponding effective fluid-surface potentials at the reduced temperature ‡ indicated to a generic Mie form.

		Free-energy average (FEA)				Unweighted average (UA1)			
Solid type	T^*	ε^*	σ^*	λ_r	λ_a	ε^*	σ^*	λ_r	λ_a
Methane-Graphene	0.8	8.1092	0.8102	9.6230	4.0680	8.1251	0.8122	9.9631	4.0187
Methane-Graphite	0.8	9.3458	0.8014	9.7325	3.7870	9.3651	0.8039	10.1555	3.7294
LJ-(111) LJ monolayer	1	4.4283	0.8187	5.5448	5.5447	4.3473	0.8587	10.0497	3.9952
LJ-(111) LJ fcc solid	1	5.3356	0.8016	5.2929	5.2928	5.2219	0.8474	10.2336	3.6784
LJ-(100) LJ monolayer	1	-	-	-	-	3.7645	0.8584	9.9847	4.0114
LJ-(100) fcc solid	1	-	-	-	-	4.7807	0.8433	10.1607	3.6429
LJ-(110) LJ monolayer	1	-	-	-	-	2.6615	0.8584	9.9596	4.0185
LJ-(110) fcc solid	1	-	-	-	-	4.0314	0.8314	10.1234	3.5249

† ε^* and σ^* are in reduced units: $\varepsilon^* = \frac{\varepsilon}{\varepsilon_{ff}}$ and $\sigma^* = \frac{\sigma}{\sigma_{ff}}$

‡ The reduced temperature is defined as $T^* = \frac{k_B T}{\varepsilon_{ff}}$

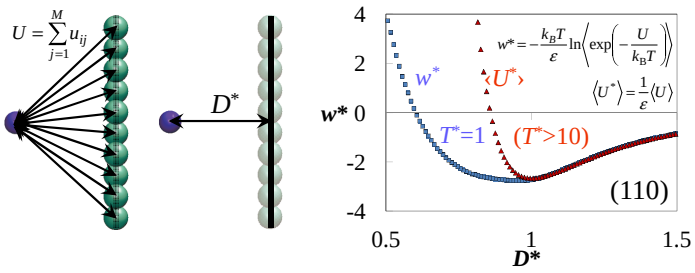

Fig. 18 Graphical Abstract